Collapse of differentially rotating neutron stars and cosmic censorship

Bruno Giacomazzo
Department of Astronomy, University of Maryland, College Park, Maryland USA and
Gravitational Astrophysics Laboratory, NASA Goddard Space Flight Center, Greenbelt, Maryland USA

Luciano Rezzolla
Max-Planck-Institut für Gravitationsphysik, Albert Einstein Institute, Golm, Germany and
Department of Physics and Astronomy, Louisiana State University, Baton Rouge, Louisiana USA

Nikolaos Stergioulas
Department of Physics, Aristotle University of Thessaloniki, Thessaloniki, Greece
(Dated: January 20, 2013)

We present new results on the dynamics and gravitational-wave emission from the collapse of differentially rotating neutron stars. We have considered a number of polytropic stellar models having different values of the dimensionless angular momentum J/M^2, where J and M are the asymptotic angular momentum and mass of the star, respectively. For neutron stars with $J/M^2 < 1$, *i.e.*, "sub-Kerr" models, we were able to find models that are dynamically unstable and that collapse promptly to a rotating black hole. Both the dynamics of the collapse and the consequent emission of gravitational waves resemble those seen for uniformly rotating stars, although with an overall decrease in the efficiency of gravitational-wave emission. For stellar models with $J/M^2 > 1$, *i.e.* "supra-Kerr" models, on the other hand, we were not able to find models that are dynamically unstable and all of the computed supra-Kerr models were found to be far from the stability threshold. For these models a gravitational collapse is possible only after a very severe and artificial reduction of the pressure, which then leads to a torus developing nonaxisymmetric instabilities and eventually contracting to a stable axisymmetric stellar configuration. While this does not exclude the possibility that a naked singularity can be produced by the collapse of a differentially rotating star, it also suggests that cosmic censorship is not violated and that generic conditions for a supra-Kerr progenitor do not lead to a naked singularity.

PACS numbers: 04.30.Db, 04.40.Dg, 95.30.Lz, 97.60.Jd

I. INTRODUCTION

Differentially rotating neutron stars, either dynamically stable or unstable, can be the result of several astrophysical scenarios such as stellar-core collapse or binary neutron star mergers (see, *e.g.* Refs. [1–11] for some recent works). Because of their differential rotation, these stars can support masses higher than if they were uniformly rotating [12]. Furthermore, if J and M are, respectively, the angular momentum and the gravitational mass of the star, differentially rotating models can reach values of the dimensionless spin parameter $J/M^2 > 1$; this is not possible for stars in uniform rotation, at least when described by a hadronic equation of state (EOS), in which case $J/M^2 \lesssim 0.7$ [13]. Finally, when hypermassive (that is, having masses larger than the one of the associated mass-shedding configuration in uniform rotation), differentially rotating stars can be related to events such as gamma-ray bursts (GRBs). Hypermassive differentially rotating neutron stars can indeed be formed after the merger of binary neutron stars and their eventual collapse can produce a spinning black hole surrounded by a hot and massive disk, which could generate the relativistic jets that are observed in short GRBs [11].

The investigation of the collapse of uniformly rotating neutron stars to rotating black holes was first studied in detail in Ref. [14], where a specific set of dynamically unstable models was constructed (named D1 to D4) for a polytropic index $N = 1$. The region of dynamical instability to axisymmetric

perturbations was probed by following the stability criterion of Friedman, Ipser, and Sorkin [15], who suggested that the turning point along constant angular-momentum sequences also marks the onset of a secular instability. Models D1 to D4 in Ref. [14] were then chosen to be near the turning-point line, but with somewhat larger central densities so as to ensure dynamical (and not just secular) instability (see Table 1 and Fig. 1 of Ref. [14])[1].

In a series of works starting with Ref. [17], the study of the collapse of differentially rotating neutron stars was initiated, both in axisymmetry and in three spatial dimensions (3D). In Ref. [17], in particular, three different models were considered, two of which were "sub-Kerr", *i.e.*, with $J/M^2 < 1$ and one was instead "supra-Kerr", *i.e.*, with $J/M^2 > 1$. The collapse of the latter was obtained by artificially depleting the pressure by 99%, but no investigation was made on the stability of the progenitor models. The results presented in [17] were based on the use of a nonconservative numerical scheme and of a polytropic EOS preventing the formation of strong shocks, which cannot be handled well by nonconservative numerical methods. In a subsequent work [18], the collapse of

---

[1] A recent investigation by Takami, Rezzolla and Yoshida [16] aimed at determining the neutral point along these sequences (*i.e.,* where the eigenfrequency of the fundamental mode goes to zero), shows however that the secular stability does not coincide with the turning point, but must be at smaller central densities.

similar models was studied in the presence of viscosity and the first results were published, but only in axisymmetry, for the collapse of differentially rotating neutron stars in the presence of a poloidal magnetic field [19–23].

The main goal of this work is to reconsider the effect of differential rotation on the collapse of rotating neutron stars and to present a systematic investigation of the stability properties of differentially rotating models. Special attention has been paid to the following two questions. (1) Do stellar models exist with $J/M^2 > 1$ and that are dynamically unstable to the collapse to black hole? (2) If a stellar model with $J/M^2 > 1$ is induced to collapse, does it lead to a naked singularity, thus violating cosmic censorship?

Overall, our results can be summarized as follows:

> *(i)* differentially rotating, sub-Kerr neutron-star models can be found that are dynamically unstable to the gravitational collapse to rotating black holes;

> *(ii)* the dynamics of sub-Kerr models is very similar to the one of uniformly rotating models: nonaxisymmetric instabilities do not have sufficient time to grow and the stars collapse promptly to black holes;

> *(iii)* the efficiency in the emission of gravitational radiation is comparable to that of uniformly rotating stars, although generically smaller since the collapse is generally slower;

> *(iv)* differentially rotating, supra-Kerr models that are dynamically unstable to the gravitational collapse to rotating black holes could not be found; rather, all of the supra-Kerr models studied were found to be dynamically stable;

> *(v)* a supra-Kerr model can be induced to collapse only through a very severe depletion of the pressure support which, however, does not lead to the prompt formation of a rotating black hole;

> *(vi)* because of the development of nonaxisymmetric instabilities, the gravitational-wave emission from supra-Kerr models could in principle be considerably larger than that of sub-Kerr models if ever induced to collapse.

The paper is organized as follows. In Sec. II we briefly summarize the equations solved and the numerical infrastructure used. In Sec. III we present our study on the stability of differentially rotating neutron stars with different degrees of differential rotation and different polytropic EOSs. In Sec. IV we present the dynamics of the collapse of four models, three with $J/M^2 < 1$ and one with $J/M^2 > 1$, and in Sec. V their gravitational-wave signal. Finally, in Sec. VI we summarize and conclude.

Throughout this paper we use a spacelike signature of $(-, +, +, +)$ and a system of units in which $c = G = M_\odot = 1$. Greek indices are taken to run from 0 to 3, Latin indices from 1 to 3 and we adopt the standard convention for the summation over repeated indices.

II. BASIC EQUATIONS AND NUMERICAL SETUP

All the simulations presented here were done using the `Whisky` code which solves the general-relativistic hydrodynamic equations on a three-dimensional numerical grid with Cartesian coordinates [24]. The code has been constructed within the framework of the `Cactus` Computational Toolkit [25], which provides high-level facilities such as parallelization, input/output, portability on different platforms and several evolution schemes to solve general systems of partial differential equations. Clearly, special attention is dedicated to the solution of the Einstein equations, whose matter terms in nonvacuum spacetimes are handled by the `Whisky` code.

In other words, while the `Cactus` code provides at each time step and on a spatial hypersurface the solution of the Einstein equations

$$G_{\mu\nu} = 8\pi T_{\mu\nu} \,, \tag{1}$$

where $G_{\mu\nu}$ is the Einstein tensor and $T_{\mu\nu}$ is the stress-energy tensor, the `Whisky` code provides the time evolution of the hydrodynamic equations, expressed through the conservation equations for the stress-energy tensor $T^{\mu\nu}$ and for the matter current density J^μ,

$$\nabla_\mu T^{\mu\nu} = 0 \,, \qquad \nabla_\mu J^\mu = 0 \,. \tag{2}$$

This system of equations is then closed by an EOS which relates the pressure to the rest-mass density and to the specific internal energy.

In what follows, and mostly for the sake of completeness, we give a brief overview of how both the right and the left-hand side of Eq. (1) are computed within the coupled `Cactus`/`Whisky` codes. The equations presented have already been discussed in several different publications, e.g. in [14, 26, 27] and we refer the interested reader to these works for more details. We note that the `Whisky` code can also solve the equations of general-relativistic magnetohydrodynamics (GRMHD) within the ideal-MHD limit [10, 11, 28]. Hereafter, however, in order to build the necessary understanding of the dynamics of gravitational collapse in the presence of differential rotation, we will consider unmagnetized fluids only, leaving the inclusion of magnetic fields to a future study.

A. Evolution of the field equations

We use the conformal and traceless decomposition of the Arnowitt-Deser-Misner (ADM) formulation [29] of the Einstein equations as first presented in 3D in Ref. [30], which is based on the ADM construction and has been further developed in [31]. Details of our particular implementation of the conformal traceless reformulation of the ADM system as proposed by [30–32] are extensively described in [26, 33] and will not be repeated here.

The code is designed to handle arbitrary shift and lapse conditions, which can be chosen as appropriate for a given spacetime simulation. More information about the possible families

of spacetime slicings which have been tested and used with the present code can be found in [26, 34]. Here, we limit ourselves to recalling details about the specific foliations used in the present evolutions. In particular, we have used hyperbolic K-driver slicing conditions of the form

$$\partial_t \alpha = -f(\alpha)\,\alpha^2 (K - K_0), \tag{3}$$

with $f(\alpha) > 0$ and $K_0 \equiv K(t=0)$, with K being the trace of the extrinsic curvature and α the lapse function. All the simulations discussed in this paper were performed using condition (3) with $f = 2/\alpha$. For the spatial gauge we use one of the "Gamma-driver" shift conditions proposed in [34] (see also [33]). In particular, all the results reported here have been obtained using the hyperbolic Gamma-driver condition,

$$\partial_t^2 \beta^i = F\,\partial_t \tilde{\Gamma}^i - \eta\,\partial_t \beta^i, \tag{4}$$

where β^i is the shift, $\tilde{\Gamma}^i$ are the "conformal connection functions" and F and η are, in general, positive functions of space and time. For the hyperbolic Gamma-driver conditions it is crucial to add a dissipation term with coefficient η to avoid strong oscillations in the shift. Experience has shown that by tuning the value of this coefficient it is possible to almost freeze the evolution of the system at late times. We typically choose $F = 3/4$ and $\eta = 3$ and do not vary them in time.

The singularity-avoiding properties of the above gauge choices have proved equally good both when using excision, as it was done in Refs. [14] and [27], and when not using excision [35]. In particular in this paper we employ the "no-excision" technique introduced in Ref. [35] and we add an artificial dissipation of the Kreiss-Oliger type [36] on the right-hand sides of the evolution equations for the field variables (no dissipation is introduced for the hydrodynamical variables). As first pointed out in Ref. [35], in fact, renouncing to excision and using instead suitable "singularity-avoiding" slicing conditions improves dramatically the long-term stability of the simulations, allowing for the calculation of the gravitational waveforms well beyond the quasi-normal-mode ringing.

B. Evolution of the hydrodynamic equations

An important feature of the Whisky code is the implementation of a *conservative formulation* of the hydrodynamic equations [37], in which the set of Eqs. (2) is written in a hyperbolic, first-order, and flux-conservative form of the type

$$\partial_t \mathbf{q} + \partial_i \mathbf{f}^{(i)}(\mathbf{q}) = \mathbf{s}(\mathbf{q}), \tag{5}$$

where $\mathbf{f}^{(i)}(\mathbf{q})$ and $\mathbf{s}(\mathbf{q})$ are the flux vectors and source terms, respectively [38]. Note that the right-hand side (the source terms) does not depend on derivatives of the stress-energy tensor.

An important feature of this formulation is that it allows for the extension to a general-relativistic context of the powerful numerical methods developed in classical hydrodynamics, in particular, high-resolution shock-capturing schemes based on exact [39–41] or approximate Riemann solvers (see Ref. [38]

for a detailed bibliography). Such schemes are essential for a correct representation of shocks, whose presence is expected in several astrophysical scenarios.

For all the results presented here, we have solved the hydrodynamic equations employing the Marquina flux formula and a third-order PPM [42] reconstruction. A third-order Runge-Kutta scheme was then used for the evolution.

C. Mesh Refinement

We solve both the spacetime and hydrodynamic equations on nonuniform grids using a "box-in-box" mesh refinement strategy implemented in Whisky via the Carpet driver [43]. This introduces two important advantages: first, it reduces the influence of inaccurate boundary conditions at the outer boundaries, which can be moved far from the central source; second, it allows for the wave zone to be included in the computational domain and thus for the extraction of important information about the gravitational-wave emission produced during the collapse. In practice, we have adopted a Berger-Oliger prescription for the refinement of meshes on different levels [44] and used the numerical infrastructure described in [43].

D. Gravitational-wave extraction

While several different methods are possible for the extraction of the gravitational-radiation content in numerical spacetimes, we have adopted a gauge-invariant approach in which the spacetime is matched with the nonspherical perturbations of a Schwarzschild black hole (see Refs. [45, 46] for applications to Cartesian coordinates). In practice, a set of "observers" is placed on 2-spheres of fixed coordinate radius $r_{\rm ex}$, where the gauge-invariant odd-parity $Q_{\ell m}^{(o)}$ and even-parity $\Psi_{\ell m}^{(e)}$ metric perturbations [47–49] are extracted. From these quantities it is possible to compute the even- and odd-parity perturbations

$$Q_{\ell m}^{+} = \lambda \Psi_{\ell m}^{(e)}, \tag{6}$$
$$Q_{\ell m}^{\times} = \lambda Q_{\ell m}^{(o)}, \tag{7}$$

where $\lambda \equiv \sqrt{2(\ell+2)!/(\ell-2)!}$. Using these quantities it is also possible to compute the gravitational-wave amplitudes in the two polarizations h_+ and $h_\times$ as

$$h_+ - {\rm i} h_\times = \frac{1}{2r} \sum_{\ell,m} \left(Q_{\ell m}^{+} - {\rm i} \int_{-\infty}^{t} Q_{\ell m}^{\times}(t')dt' \right) {}_{-2}Y^{\ell m}, \tag{8}$$

where ${}_{-2}Y^{\ell m}$ are the $s = -2$ spin-weighted spherical harmonics. We note that the approach discussed above cannot be employed when simulating the supra-Kerr model, for which a very high resolution is necessary and hence the use of a computational domain with rather close boundaries. As we will comment later on in Sec. V B, for that model the gravitational-wave emission will be computed through the quadrupole formula.

III. INITIAL STELLAR MODELS

A. Equation of state and differential-rotation law

We construct our initial stellar models using the numerical code rns [50] (see [51, 52] for evaluations of its accuracy) as isentropic, differentially rotating relativistic polytropes, satisfying the polytropic EOS

$$p = K\rho^{\Gamma}, \tag{9}$$

$$e = \rho + \frac{p}{\Gamma - 1}, \tag{10}$$

where p, ρ, and e are pressure, rest-mass density, and energy density, respectively, while $K = 100$ and Γ are the polytropic constant and the polytropic exponent, respectively. In our discussion we will also use the polytropic index N, defined through the relation $\Gamma \equiv 1 + 1/N$.

We further assume that the equilibrium models are stationary and axisymmetric, so that the spacetime geometry is described by a metric of the form

$$ds^2 = -e^{2\nu}dt^2 + e^{2\psi}(d\phi - \omega dt)^2 + e^{2\mu}(dr^2 + r^2 d\theta^2), \tag{11}$$

where ν, ψ, μ and ω are functions of the quasi-isotropic coordinates r and θ only. The degree of differential rotation, as well as its variation within the star, are essentially unknown and because of this we here employ the well-known "j-constant" law of differential rotation [53]

$$A^2(\Omega_c - \Omega) = \frac{(\Omega - \omega)e^{2\psi}}{1 - (\Omega - \omega)e^{2\psi}}, \tag{12}$$

where $\Omega \equiv \Omega(r, \theta)$ is the angular velocity, Ω_c is the angular velocity at the center of the star, and A is a constant (with the dimensions of length) that represents the lengthscale over which the angular velocity changes (see [54] for a new and more realistic law of differential rotation). In the remainder of this Section, we will measure the degree of differential rotation by the rescaled quantity $\hat{A} \equiv A/r_e$, where r_e is the equatorial coordinate radius of the star. For $\hat{A} \to \infty$ uniform rotation is recovered while a low value of $\hat{A}$ indicates a high degree of differential rotation.

B. Equilibrium models

As mentioned in the introduction, when studying the gravitational collapse of a rotating neutron star to a Kerr black hole, an interesting question is about what happens to a configuration with an initial dimensionless spin parameter $J/M^2 > 1$ (*i.e.*, a supra-Kerr model). If the cosmic censorship conjecture is expected to hold, such models cannot collapse promptly to Kerr black holes, which are limited to $J/M^2 \leq 1$. Rather, one expects that the transition to a black hole, when it occurs, takes place after the stellar model has shed some of its angular momentum. This was indeed what was shown to happen

in the previous study of Ref. [17], where a dynamically stable supra-Kerr model was induced to collapse after a dramatic depletion of the pressure support.

Here, we consider again this interesting question but, before discussing in more detail the features of the gravitational collapse of either supra- or sub-Kerr models, it is worth discussing the properties of the equilibrium models that can be computed with the prescriptions of the EOS and of the differential-rotation law discussed in the previous section III A. As will become apparent, the study of these equilibrium models will be quite revealing for the stability properties and hence for what is realistic to expect from the gravitational collapse of differentially rotating neutron stars. To this end, we have constructed a large set of initial models for various values of the polytropic index N and degree of differential rotation $\hat{A}$, reaching close to the mass-shedding limit and spanning a wide range of central densities.

Figure 1 shows the value of J/M^2 as a function of central rest-mass density ρ_c for the three different EOSs with $N = 0.5$, $N = 0.75$, and $N = 1.0$. In these sequences the rotation law and the polar-to-equatorial coordinate axis ratio are fixed to $\hat{A} = 1.0$ and $r_p/r_e = 0.35$, respectively. The choice of $\hat{A} = 1.0$ is a typical one, representing moderate differential rotation (the angular velocity at the axis and at the equator differ by a factor of ~ 3), while the axis ratio of 0.35 refers to very rapidly rotating models near the mass-shedding limit (when the limit exits). Along each sequence, we mark by a filled circle the model which roughly separates stable models (at lower central rest-mass densities) from unstable models (at higher central rest-mass densities). As we do not know precisely which are the marginally stable models (no simple turning-point criterion exists in the case of differential rotation), we use as a reference the stability limit of the nonrotating models and thus we mark with a circle the central rest-mass density of the nonrotating model having the maximum mass for each EOS[2]. Stated differently, all models to the right of the circles are expected to be dynamically unstable or at least very close to the instability threshold.

As becomes clear from this figure, all *unstable models* we were able to construct have $J/M^2 < 1$, *i.e.*, are sub-Kerr. In contrast, in order to find supra-Kerr models, one must reach very low central rest-mass densities, where equilibrium models are instead expected to be (very) stable against axisymmetric perturbations. Interestingly, for the particular sequences considered here, the value of J/M^2 in the unstable region (*i.e.*, to the right of the filled circles) becomes nearly constant for all the considered values of the polytropic indices considered; this represents an additional evidence that all unstable models are indeed sub-Kerr.

---

[2] We also note that the value of the central rest-mass density separating stable from unstable models in the case of uniformly rotating neutron stars changes by less than $\approx 5\%$ when moving from a nonrotating sequence to a maximally rotating one. As a result, using a nonrotating model to mark the stability is a very good approximation which does not affect the results presented here.
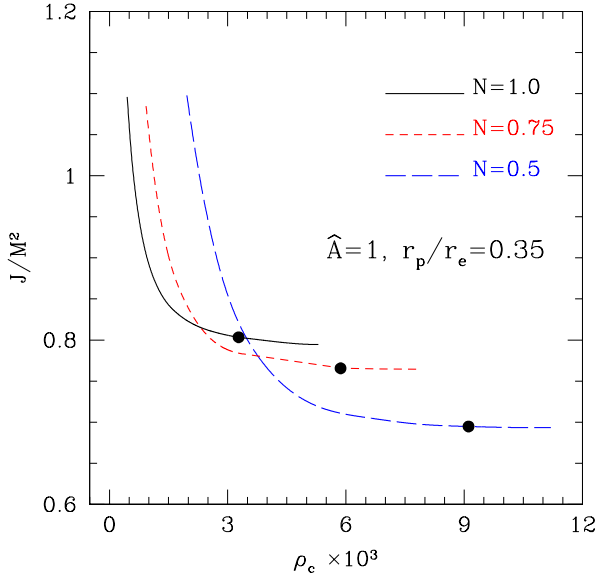
FIG. 1: J/M^2 as a function of central rest-mass density ρ_c for models with polytropic indices $N = 0.5$, $N = 0.75$ and $N = 1.0$, when the rotation law and the polar-to-equatorial coordinate axis ratio are fixed to $\hat{A} = 1.0$ and $r_p/r_e = 0.35$, respectively. The circle denotes roughly the separation between stable (at the left of the circle) and unstable (at the right) models along each sequence.
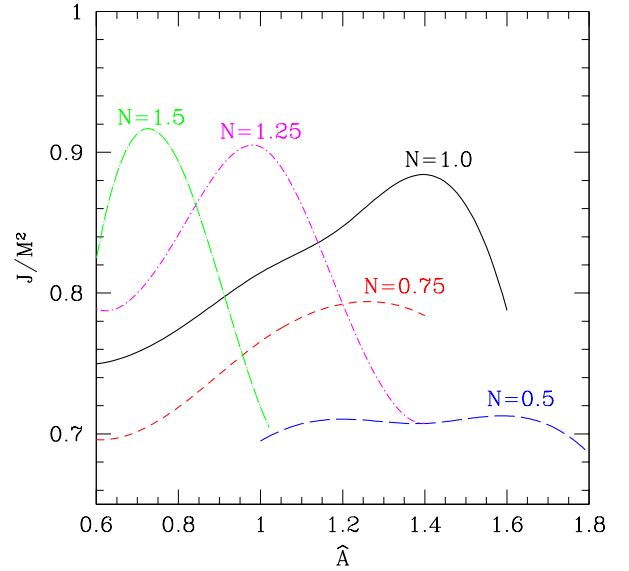
FIG. 2: J/M^2 of the most rapidly rotating models with a central rest-mass density equal to that of the maximum-mass nonrotating models (*i.e.*, for the models marked with the circles in Fig. 1) as a function of the rotation law parameter $\hat{A}$ and for different values of N. All models have $J/M^2 < 1$ indicating the difficulty of constructing unstable supra-Kerr models.

In order to investigate further the effect of the differential-rotation-law parameter $\hat{A}$ and of the EOS on the above conclusion, we have investigated a large number of rapidly rotating models, spanning a wide range of values for $\hat{A}$ (between 0.6 and 1.8) and a wide range of polytropic indices (between 0.5 and 1.5). In all cases, we have computed the value of J/M^2 of the most rapidly rotating models we could construct (which was normally close to the mass-shedding limit, when it exists) for a central rest-mass density equal to that of the maximum-mass nonrotating model (*i.e.*, for the models marked by circles in Fig. 1). The results of this analysis are collected in Fig. 2, which shows that all the models with a central density equal to the maximum-mass nonrotating stars have $J/M^2 < 1$, when N and $\hat{A}$ are allowed to vary. This remains true also when considering the unstable models in Fig. 1 (*i.e.*, the ones with an higher central density), which all have a value of J/M^2 lower than the models shown in Fig. 2. It is therefore evident that no combination of N and $\hat{A}$ could yield an unstable supra-Kerr model. All of these results provide strong evidence that all *supra-Kerr models* examined here *are stable*.

Bearing this in mind, it should be noted that because our numerical method does not reach exactly the mass-shedding limit for any degree of differential rotation (it is difficult to achieve convergence at very small values of the axis ratio r_p/r_e) and since the existence of a bifurcation between quasi-

spheroidal and quasitoroidal models[3] with the same axis ratio and central density has not been investigated yet, we cannot strictly exclude the existence of supra-Kerr unstable models.

The rapidly rotating models with $N = 1.0$, $N = 0.75$ and $N = 0.5$ shown in Fig. 1 are also shown in Fig. 3 in a mass vs maximum energy density plot. Since the most rapidly rotating models with differential rotation and small axis ratio are quasitoroidal, the corresponding maximum energy density is larger than the central energy density by a factor of roughly 2, depending on the degree of differential rotation. It is not yet known whether the value of the central energy density or of the off-center maximum energy density is more important in determining the stability to axisymmetric perturbations of quasitoroidal models. Therefore, the models shown in Figs. 2 and 3 could either be only marginally stable or unstable or strongly unstable. Nevertheless, the fact that the central density of models in Fig. 1 with $J/M^2 > 1$ is at least a factor of 3 smaller than the central density of the corresponding maximum-mass nonrotating models, indicates that even if all models in Fig. 3 are well inside the dynamically unstable region, there should still be no supra-Kerr unstable models for the parameter range examined.

---

[3] We define as "quasi-spheroidal" those models having the central and maximum rest-mass density being coincident, while we define as "quasi-toroidal" those models having the maximum of the rest-mass density not located at the center of the star.

TABLE I: Initial data for the different stellar models. The different columns refer, respectively, to the central rest-mass density ρ_c and its maximum ρ_{max}, the ratio of the polar to the equatorial coordinate radii r_p/r_e, the total gravitational mass M, the circumferential equatorial radius R_e, the central angular velocity Ω_c, the ratio of rotational kinetic energy to gravitational binding energy $T/|W|$, the ratio J/M^2, where J is the angular momentum, and the degree of differential rotation $\hat{A}$, where for $\hat{A} \to \infty$ uniform rotation is recovered. All the initial models have been computed with a polytropic EOS with $K = 100$ and $N = 1$. The last column shows instead the ratio J_{BH}/M_{BH}^2 for the BH formed after the collapse of the Sub-Kerr models computed using Eq. (5.2) in Ref. [14].

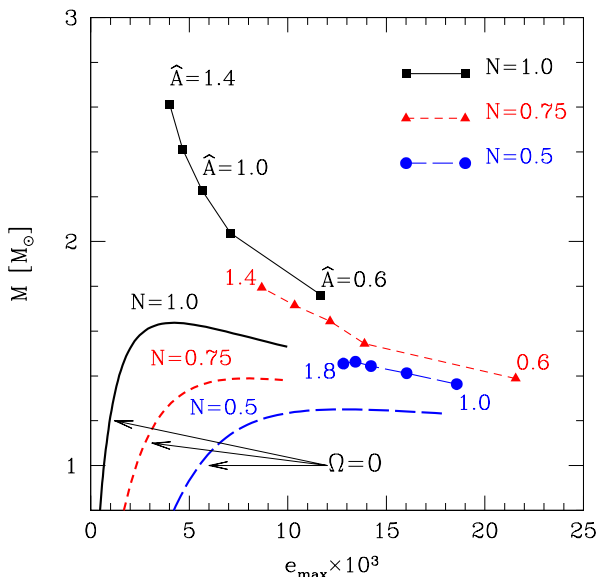| Model	$\rho_c \times 10^{-3}$	$\rho_{max} \times 10^{-3}$	r_p/r_e	$M/M_\odot$	R_e/M	Ω_c	$T/|W|$	J/M^2	$\hat{A}$	J_{BH}/M_{BH}^2
A1	3.0623	6.8920	0.23	1.7626	3.5424	0.51891	0.18989	0.75004	0.6	0.74
A2	3.0623	4.0236	0.33	2.2280	3.5316	0.21752	0.21705	0.81507	1.0	0.81
A3	3.0623	3.0623	0.33	2.6127	4.1111	0.10859	0.23163	0.88474	1.4	0.88
B1	0.4630	0.4632	0.39	1.9009	8.8185	0.03723	0.21509	1.08650	1.0	

FIG. 3: The solid, short-dashed and long-dashed lines (upper curves with individual models marked) represent the gravitational mass M of some of the unstable models shown in Fig. 2, as a function of the maximum energy density, for $N = 0.5, 0.75$ and 1.0. The different values of $\hat{A}$ are reported near each model. The lower curves show the corresponding nonrotating sequence of models for each of the above EOSs.
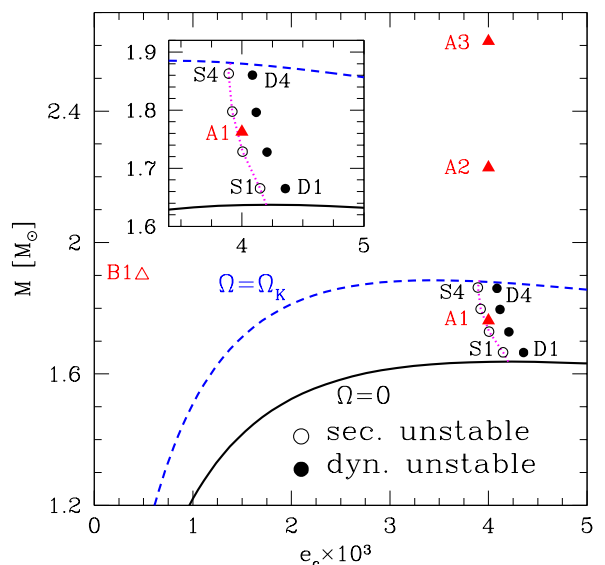
FIG. 4: Comparison between our initial models (filled triangles; see Table I) and the uniformly rotating models studied in Ref. [14]. Here we plot the gravitational mass M as a function of the central energy density e_c. The solid, dashed, and dotted lines correspond to the sequence of nonrotating models, the sequence of models rotating at the mass shedding limit, and the sequence of uniformly rotating models that are at the onset of the secular instability to axisymmetric perturbations. Also shown are the secularly (open circles) and dynamically unstable (filled circles) initial models used in Ref. [14] (see inset).

C. Supra- and sub-Kerr initial data

We have investigated the dynamics of differentially rotating collapsing compact stars by focusing on three sub-Kerr, dynamically unstable models and on one supra-Kerr, dynamically stable model. For the latter, the collapse was triggered through an artificially large pressure depletion of 99%, as was done in Ref. [17]. All models are constructed with the polytropic EOS with $N = 1$ and $K = 100$. The three dynamically unstable models are labeled A1 to A3 and are shown as filled triangles in Fig. 4 while their detailed properties are displayed in Table I. The central rest-mass density of the three models is chosen to be the same as the central rest-mass density of the maximum mass nonrotating model for this EOS. The degree of differential rotation varies from $\hat{A} = 0.6$ to $\hat{A} = 1.4$. The maximum rest-mass density increases with respect to the central density, as differential rotation becomes stronger (*i.e.*, as the relative length scale $\hat{A}$ becomes smaller), as can be seen by comparing the values in the second and third columns of Table I. All three models have comparable values of J/M^2 (0.75 to 0.88), of the ratio of rotational kinetic energy to gravitational binding energy $T/|W|$ (0.19 to 0.23) and of the total (gravitational) mass M (1.8 to 2.6), while they differ significantly in radius (6.4 to 11) and central angular
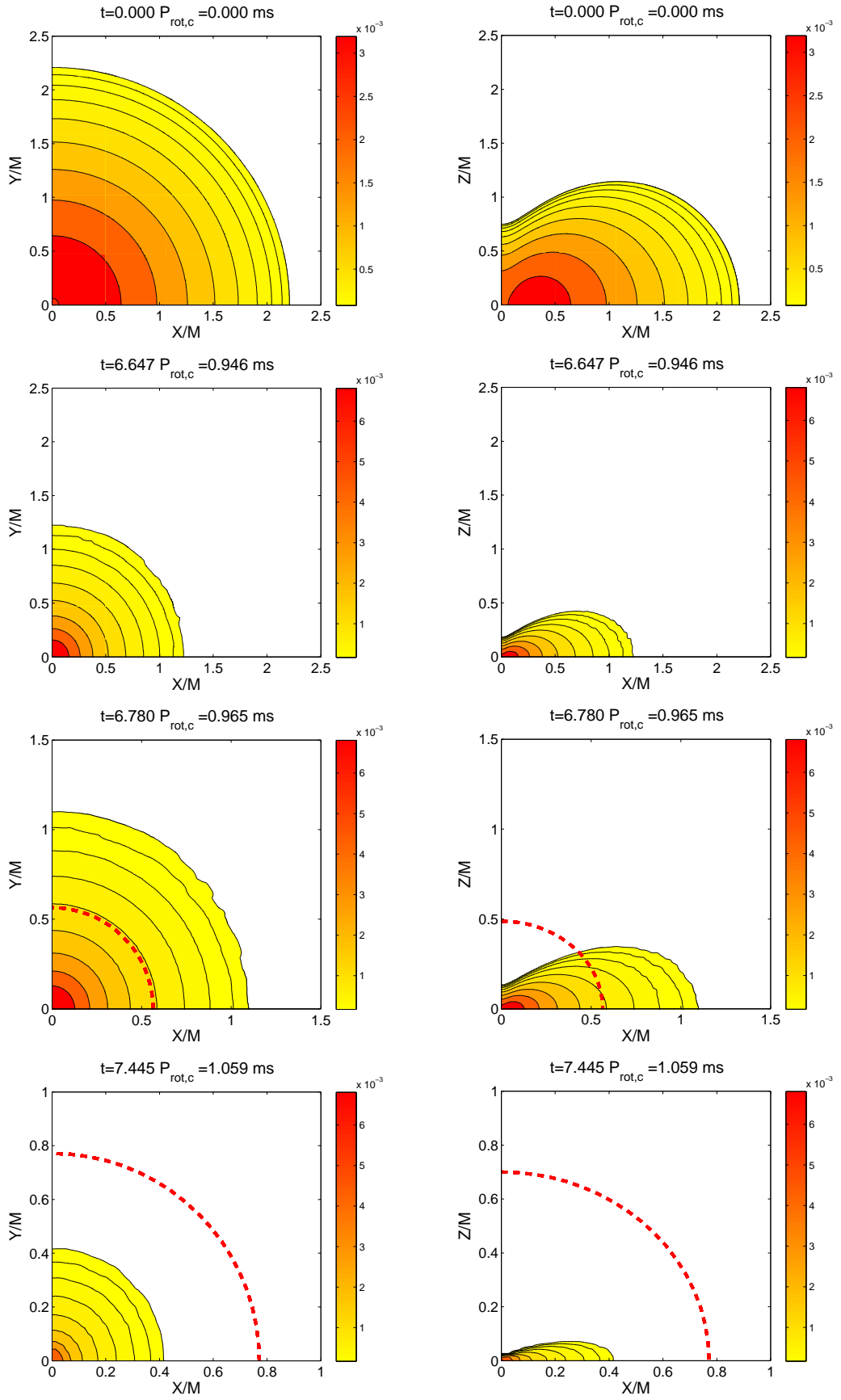
FIG. 5: Snapshots of the rest-mass density ρ in the equatorial plane (left panels) and in the xz plane (right panels) for model A2. The contour lines are drawn for $\rho = 10^{-(0.2j+0.1)}\rho_{\max}$ for $j = 0, 1, \ldots, 8$, where $\rho_{\max}$ is the maximum of ρ. After the formation of the AH (dashed line) at time $t_{\mathrm{ah}} = 6.71 P_{\mathrm{rot,c}}$, $\rho_{\max}$ is the maximum of ρ at $t = t_{\mathrm{ah}}$. Time is normalized to the initial central rotation period of the star, $P_{\mathrm{rot,c}} = 13M$.

velocity (0.52 to 0.11). Even though the axisymmetric stability of these models cannot be determined from a turning-point method, the numerical simulations performed and discussed later on, showed that these models are indeed dynamically unstable and collapse without the need of a pressure depletion.

Finally, the fourth model studied, model B1 in Table I, is shown as a empty triangle in Fig. 4 and represents a stable supra-Kerr model, with comparable mass and $T/|W|$-ratio as models A1 to A3, but with much smaller central rest-mass density and $J/M^2 = 1.09$. The complete set of initial data is displayed in Fig. 4, which reports the total mass versus the energy density at the center of the star e_c. Also shown as useful references are the sequence of nonrotating models (solid line), the sequence of models rotating at the mass-shedding limit (dashed line) and the sequence of models that are at the onset of the secular instability to axisymmetric perturbations (dotted line). Similarly, indicated respectively with open and filled circles, are the secularly (S1 − S4) and dynamically unstable (D1 − D4) uniformly rotating models used in the collapse simulations discussed in Ref. [14] (see Fig. 4 inset).

IV. DYNAMICS OF THE COLLAPSE

We next discuss the dynamics of the matter during the collapse of the initial stellar models described in the preceding section. All the models were studied with different resolutions and using fixed mesh refinement techniques. In the case of the sub-Kerr models A1, A2, and A3, up to seven refinement levels were used, in order to be able to extract the gravitational-wave signal in a region sufficiently distant from the sources.

The supra-Kerr model B1, on the other hand, was studied using three levels because the dynamics is not limited to a small central region of the computational domain (the process follows several bounces and subsequent collapses) and so the finest refinement level was set to be larger with respect to the one used for the sub-Kerr models in order to reduce the numerical error. The outer boundaries were then moved at those distances that were computationally affordable, but not sufficiently far away to allow for gravitational-wave extraction as in the sub-Kerr cases. For this model, in fact, we resort to a gravitational-wave extraction via the quadrupole formula, as discussed in Sec. V B.

An ideal-fluid EOS, $P = \rho\epsilon(\Gamma - 1)$, with $\Gamma = 2$ was used during the evolution of all the models.

A. Sub-Kerr Collapse

All the three sub-Kerr models considered A1, A2, A3 show the same qualitative dynamics, with the gravitational collapse leading to a central black hole. All of them were evolved in equatorial and $\pi/2$ symmetry (*i.e.*, we considered the region $\{x > 0, y > 0, z > 0\}$ applying reflection symmetry at $z = 0$ and a rotational symmetry at $x = 0$ and $y = 0$) since they did not show the development of nonaxisymmetric instabilities (when evolved without symmetries at lower resolutions),
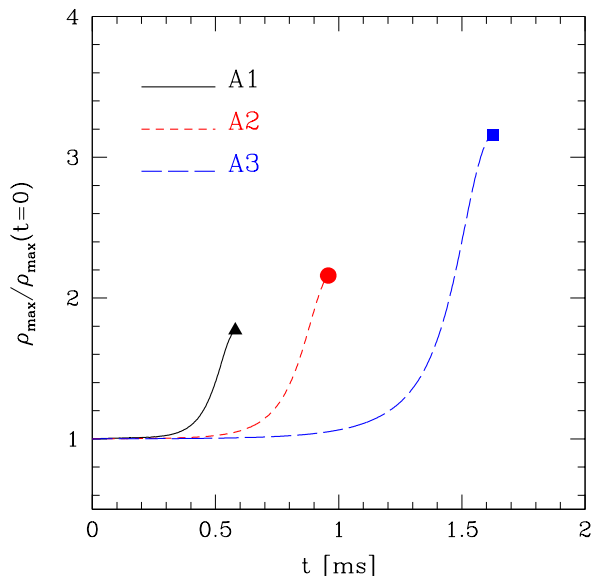

FIG. 6: Maximum of the rest-mass density ρ normalized to its initial value. The triangle, the circle and the square represent the moment at which an apparent horizon is formed for models A1, A2, and A3, respectively. This figure should be compared with the corresponding Fig. 10, which refers to the supra-Kerr model B1.

in a way similar to the uniformly rotating models studied in Ref. [14].

Because of the similar behavior, we concentrate here only on the description of model A2. The results shown here were produced on a grid with boundaries located at $[0, 137.9M] \times [0, 137.9M] \times [0, 137.9M]$ with a resolution ranging from $\Delta x^i = 0.86M$ on the coarsest grid to $\Delta x^i = 0.013M$ on the finest one, using seven refinement levels. The boundaries of the finest grid were chosen in order to include all the star and thus to reduce numerical errors. The results shown here were obtained without the introduction of any initial perturbation, except from the truncation error, but a similar dynamics was obtained when the collapse was triggered by reducing the pressure by 2%, as was done in the case of uniformly rotating models in Ref. [14].

As one can see in the first row of panels in Fig. 5, where we show the isodensity contours in the (x, y) (*i.e.*, equatorial) and (x, z) planes, the star has a toroidal shape due to its strong differential rotation. Its evolution is rather similar to what was already observed for the uniformly rotating models and especially for model D4 in Ref. [14]. The collapse is axisymmetric and leads to the formation of a black hole, as indicated by the appearance of an apparent horizon (AH) [55]. The AH, represented by a dashed line in Fig. 5, is found at $t = 6.71P_{\rm rot,c}$, where $P_{\rm rot,c}$ is the initial rotational period at the center of the star and is equal to $\simeq 13M$. At the time the AH is formed, the star has assumed the shape of a disk which rapidly accretes until no matter is left outside, as one can see from the last row of panels in Fig. 5. Even if we used an ideal-fluid EOS, we did not see the formation of global shocks during the collapse.
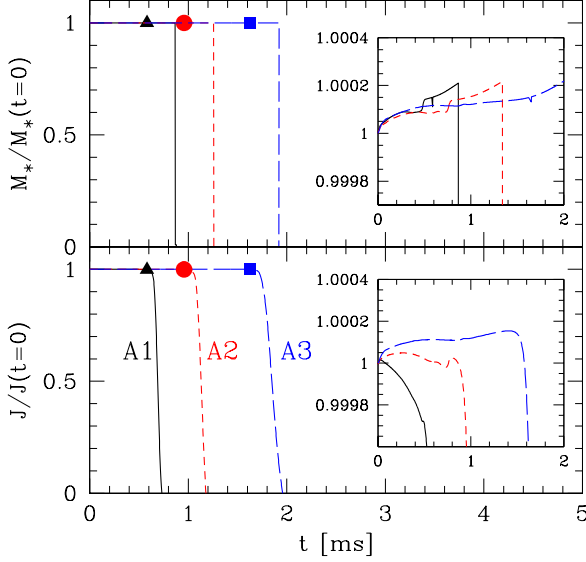
FIG. 7: Total rest-mass M_* and angular momentum J of the matter, normalized at $t = 0$ for the three different models A1 (solid line), A2 (short-dashed line), and A3 (long-dashed line). The triangle, the circle, and the square represent the moment at which an apparent horizon is formed for, respectively, model A1, A2, and A3.

In Fig. 6 we plot instead the maximum of the rest-mass density normalized at its initial value for all the three sub-Kerr models. All the models show the same dynamics with an exponential increase in the maximum of the rest-mass density and with the AH forming when ρ_{max} has reached a value ~ 2 times larger than the initial one. As expected, models with a higher value of J/M^2 collapse on a longer timescale.

In Fig. 7 we compare the total rest-mass and the total angular momentum of all the three models (A1, A2, A3) normalized to their initial values. As one can see from this figure, the level of accuracy for these simulations is very high, with a relative error in the conservation of rest-mass and angular momentum smaller than 10^{-3}. Note also that the angular momentum is computed from the matter sources, outside the apparent horizon, and hence it is shown to vanish at late times in Fig. 7, as the matter is dissipated near the singularity (see discussion in [35, 56]).

B. Supra-Kerr Collapse

Model B1 has $J/M^2 \simeq 1.1$ and shows very different dynamics with respect to the sub-Kerr models. Because in this case we expected the development of nonaxisymmetric instabilities, we decided to adopt equatorial and π-symmetry (this means that we evolved only the region $\{x > 0, z > 0\}$ applying a rotational symmetry boundary condition at $x = 0$ and reflection symmetry at $z = 0$). Here we report the results obtained on a grid with boundaries located at $[0, 34M] \times [-34M, 34M] \times [0, 34M]$ and with a resolution

ranging from $\Delta x^i = 0.17M$ to $\Delta x^i = 0.04M$ with three refinement levels and with the finest grid covering the entire star. It is worth remarking that the resolutions adopted here for the supra-Kerr model are considerably finer than the ones routinely adopted in the simulation of binary neutron stars (see, e.g., [4, 10, 11, 57]), and of a factor $\simeq 4$ larger. As a result, although this scenario is much simpler to simulate, its computational costs are indeed equally high.

Because model B1 is a very stable configuration, we had to enforce its collapse by artificially reducing the initial pressure by 99%, as was done by Duez et al. [17], while smaller pressure reductions were found to be insufficient to trigger the collapse. With its pressure support removed, the model immediately flattens along the z-direction and collapses toward the center on the equatorial plane, producing a strong shock. After a first bounce, due to the centrifugal barrier produced by the large angular momentum, a quasitoroidal structure forms, which rapidly fragments into four clumps (see the snapshots from time $t = 1.122P_{rot,c}$ to $t = 2.154P_{rot,c}$ in Fig. 8) whose formation was observed also in Ref. [17]. We have also extracted the Fourier modes of the rest-mass density ρ, by computing at $z = 0$ and at different cylindrical radii $\varpi \equiv \sqrt{x^2 + y^2}$, the averages

$$k_m(\varpi') \equiv \int_{z=0,\varpi'} \rho(\varpi'\cos(\phi), \varpi'\sin(\phi))e^{im\phi}d\phi. \quad (13)$$

The mode power P_m is then simply given by

$$P_m \equiv \frac{1}{\varpi_{out} - \varpi_{in}} \int_{\varpi_{in}}^{\varpi_{out}} |k_m(\varpi)|d\varpi, \quad (14)$$

where ϖ_{in} and ϖ_{out} are chosen to cover the whole domain (for details and an extensive use of this technique, see also Refs. [58, 59]).

The presence of an $m = 4$ mode at the beginning can be then seen looking also at the modes' power plotted in Fig. 9, where we show the evolution of the $m = 2$ (solid line) and $m = 4$ (dashed line) modes, being the other modes either zero or much smaller during the entire simulation. It is not clear at the moment whether the fragmentation has to be considered physical and only triggered by the use of a Cartesian grid, or entirely due to our Cartesian coordinate system. We note that Truelove and collaborators [60] have shown that spurious fragmentation can occur if the Jeans length is not well resolved, i.e. if the following "Jeans condition" is verified,

$$\frac{\Delta x}{\lambda_J} \gtrsim \frac{1}{4}, \quad (15)$$

where λ_J is the Jeans length and is given by

$$\lambda_J \approx \sqrt{\left(\frac{\pi c_s^2}{\rho}\right)} \quad (16)$$

and c_s is the sound speed. Duez et al. [17] estimated the minimum of the Jeans length to be $\lambda_J \approx 1.3M$ for a model similar to our model B1 and using a polytropic EOS (for an ideal-fluid EOS, as the one used in our simulations, the sound speed
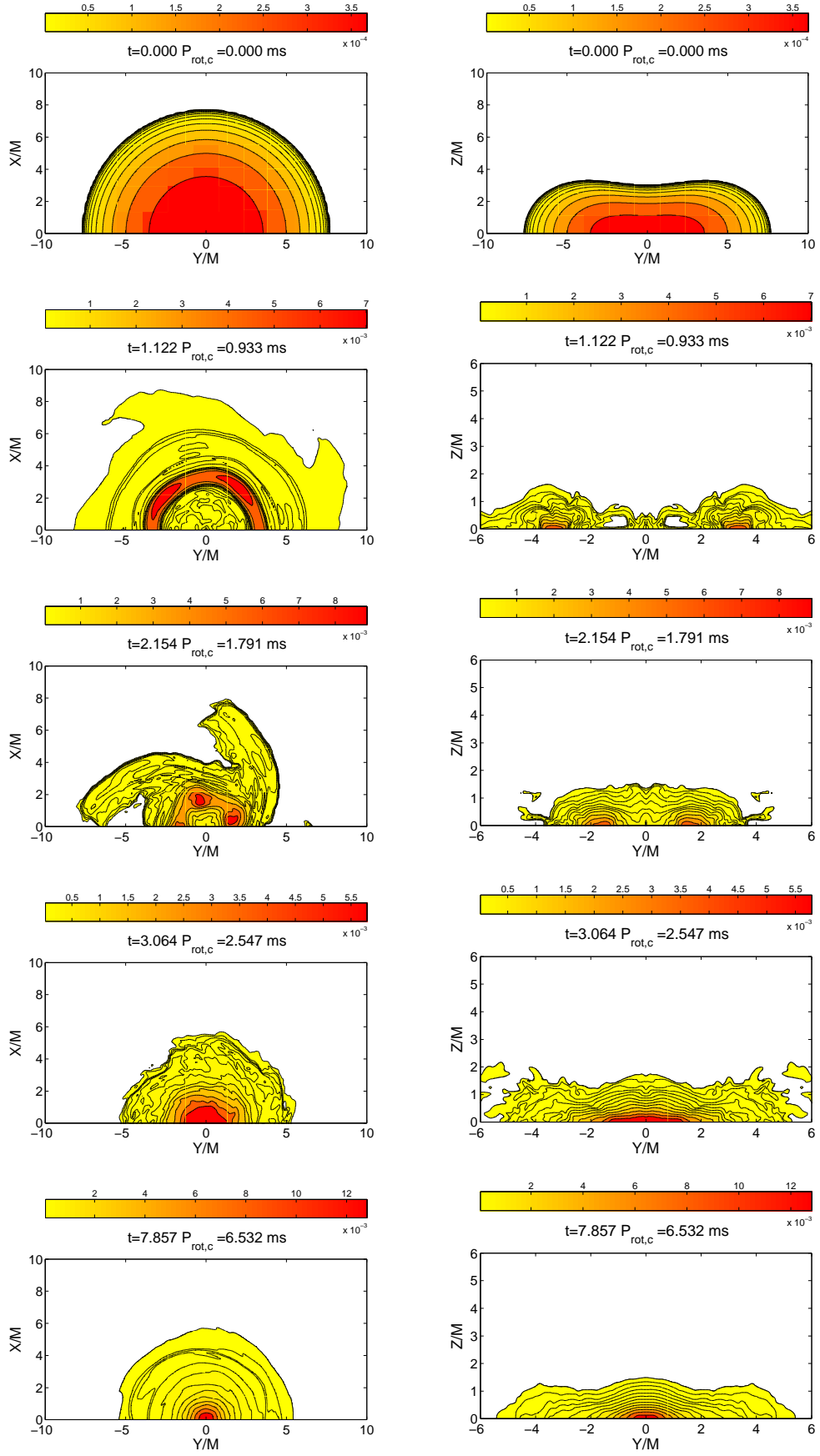
FIG. 8: Snapshots of the rest-mass density ρ in the equatorial xy plane (left panels) and yz plane (right panels) for model B1. The contour lines are drawn for $\rho = 10^{-(0.2j+0.1)} \max(\rho)$ for $j = 0, 1, \ldots, 12$. Time is normalized to the initial central rotational period of the star, $P_{\text{rot},c} = 89M$.
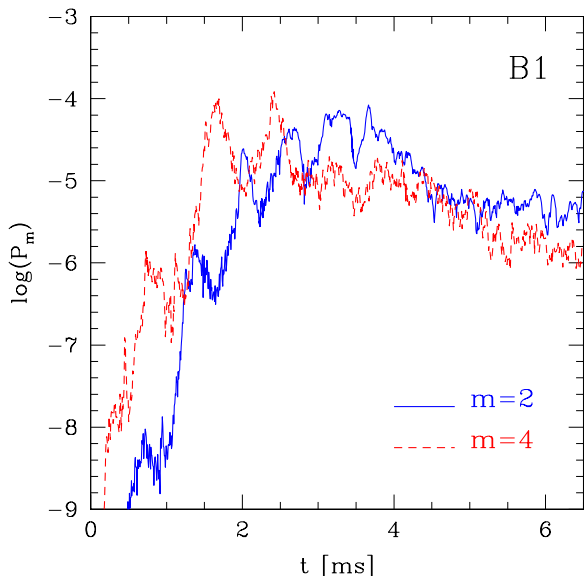
FIG. 9: Logarithm of the power in the $m = 2$ (solid line) and $m = 4$ (dashed line) Fourier modes as a function of time for model B1. The modes not shown in this plot are zero during all of the evolution.

FIG. 10: The maximum value of rest-mass density ρ and of the specific internal ϵ normalized to their initial value and during the evolution of the supra-Kerr model B1. Note that the end-configuration is that of equilibrium, with larger central density and internal energy. This figure should be compared with the corresponding Fig. 6, which refers to the sub-Kerr models A1 − A3.

is generically larger). In the simulation of Duez et al. [17], but also in ours, the value of $\Delta x/\lambda_J$ is indeed found to be smaller than 0.25, leading to the conclusion that the fragmentation is physical and due to a genuine nonaxisymmetric instability. We should remark, however, that in Ref. [60] the condition (15) was indicated as necessary but not in general sufficient to avoid the formation of spurious fragmentation. Thus, even if the resolutions used in our simulation and in the one reported in Ref. [17] satisfy the Jeans condition, we cannot thus strictly exclude that the origin of this $m = 4$ mode is due to the use of a Cartesian grid. Further investigations with resolutions higher than the ones that could be afforded here and with different coordinate systems will be necessary in order to clarify this issue.

At time $t \approx 2.5 P_{\mathrm{rot,c}}$ the four fragments merge and a new collapse and bounce follows with the formation of a new quasitoroidal structure. The effects of these bounces on the maximum of the rest-mass density ρ and specific internal energy ϵ are shown in Fig. 10. At $t \approx 3.0 P_{\mathrm{rot,c}}$ the quasitoroidal structure contracts toward the center, forming a new configuration which does not collapse further, but that develops a bar which lasts for ≈ 2 ms. At this point, the model approaches a new stable configuration, as one can easily see from the worldline of the maximum of the rest-mass density ρ (Fig. 11) and from its evolution (Fig. 10, top panel). It is also evident from Fig. 9 that at late times the $m = 2$ mode dominates.

In Fig. 12 we plot the evolution of the total rest-mass and of the total angular momentum normalized to their initial values. When we stopped the simulation, J had dropped by $\sim 10\%$. The loss in the angular momentum cannot be accounted for in full by the emission of gravitational waves and it is due to the loss of mass, which is expelled by shocks through the external
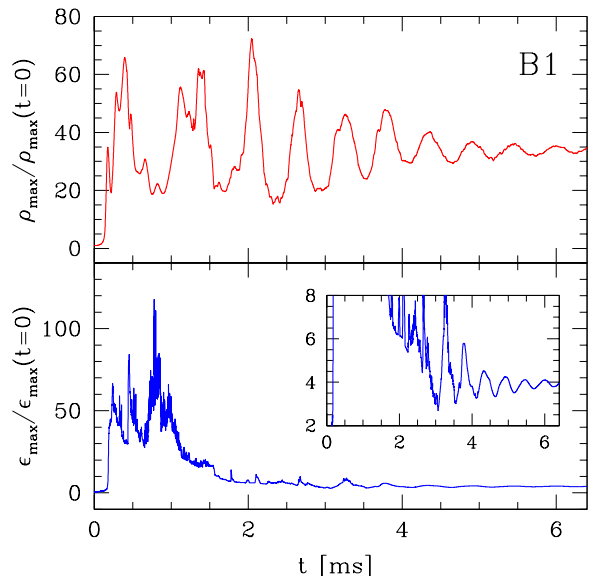
boundaries. In the inset of Fig. 12 we plot instead the profiles of the angular velocity along the x-axis, $\Omega = (\alpha v^y - \beta^y)/x$ at the initial time (purple long-dashed line) and at the end of the simulation (light blue solid line), and where v^j is the three-velocity of the fluid as measured by an Eulerian observer [14]. For comparison we also show the Keplerian profile $\Omega_K \propto r^{-3/2}$ (black short-dashed line). It is evident that the collapse leads to an even larger degree of differential rotation than the initial one and that the new equilibrium is very close to a Keplerian configuration in its outer layers. This is clearly the result of having essentially removed pressure forces, leaving the centrifugal ones the only ones responsible for the equilibrium.

As a final remark we note that the fact that we were not able to force this model to collapse to a black hole, even when artificially reducing the pressure by 99%, confirms that supra-Kerr models cannot directly collapse to a black hole. Furthermore, the evidence that even when forced to collapse the supra-Kerr model does not produce a black hole, but rather redistributes its angular momentum to reach a stable and axisymmetric stellar configuration, provides strong evidence that cosmic censorship is not violated and that rather generic conditions for a supra-Kerr progenitor do not lead to a naked singularity.

V. GRAVITATIONAL-WAVE EMISSION

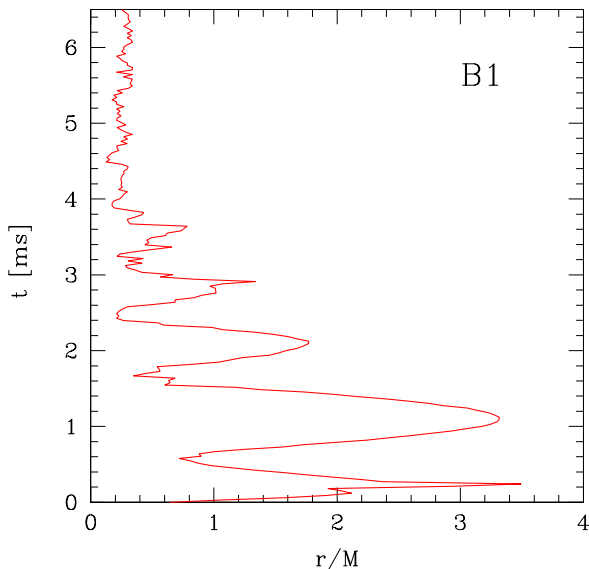We now concentrate on the emission of gravitational waves from the sub-Kerr and supra-Kerr models, with the aim of

FIG. 11: Worldline of the maximum of the rest-mass density ρ for model B1. The final configuration has a maximum located at a radius smaller than the initial one. Note also the three bounces.

comparing our results with those obtained in Refs. [27, 61] for the collapse of uniformly rotating neutron stars models.

A. Sub-Kerr Models

In Fig. 13 we show h_+ and $h_\times$ for the A2 sub-Kerr model. We recall that in the case of axisymmetric collapse to black hole (BH) the signal is expected to be composed by an initial rapid increase in the amplitude, due to the initial phase of the collapse, followed by a ring-down phase of the formed BH [27, 35, 61–64]. These two phases are very evident in Fig. 13 and the same behavior is shown also by the other sub-Kerr models. The initial oscillations visible in the h_+ for the first 0.5ms are spurious effects related to the initial violation of the Hamiltonian constraint introduced by importing axisymmetric models computed on a spherical grid onto the Cartesian grid used for the evolution. We have verified indeed that these oscillations decrease in amplitude with increasing resolution, while the rest of the signal remains the same.

In Table II we report the signal-to-noise ratio for various second and third-generation gravitational-wave detectors and the energy emitted through gravitational waves for all the sub-Kerr models, assuming a galactic source at a distance of 10 kpc. For example, gravitational waves from the collapse of model A2, with a total energy of about $1.4 \times 10^{-7}M$, would arrive at the Virgo detector with a signal-to-noise ratio of $S/N \approx 2.11$ (with a characteristic amplitude of $h_c = 6.14 \times 10^{-21}(M/M_\odot)$ and at a characteristic frequency $f_c = 1367$Hz). In the case of LIGO, instead, we obtain $h_c = 5.28 \times 10^{-21}(M/M_\odot)$ at $f_c = 1133$Hz with $S/N \approx 1.5$ while for advanced LIGO we have $h_c = 3.81 \times 10^{-21}(M/M_\odot)$
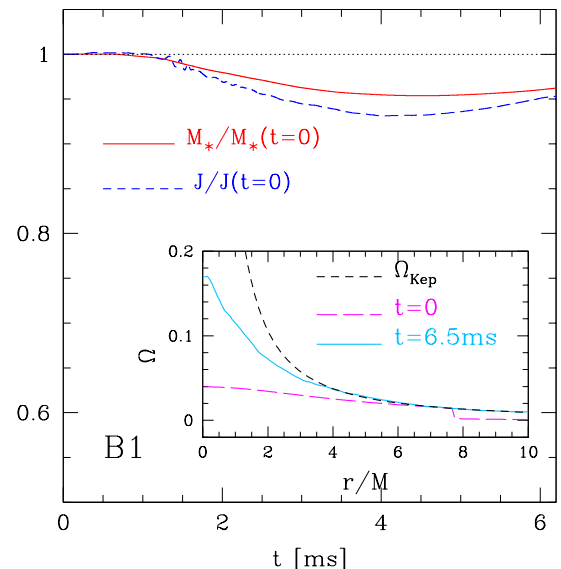

FIG. 12: Total rest-mass M_* and total angular momentum J normalized at their initial values for the supra-Kerr model B1. The inset shows instead the profiles of the angular velocity Ω at the initial time (purple long-dashed line) and at the end of the simulation (light blue solid line). For comparison we also show the Keplerian profile $\Omega_K \propto r^{-3/2}$ (black short-dashed line).

at $f_c = 809$Hz with $S/N \approx 14.7$. However, when consider third-generation detectors such as the Einstein Telescope (ET) [65], the signal-to-noise ratio would increase dramatically to $S/N \approx 247$ and the source could then be detected up to a distance of ~ 1 Mpc. Even though detection of individual events is difficult, the case of a stochastic background is worth further investigation.

The gravitational-wave energies computed here are similar to those obtained for the collapse of uniformly rotating neutron stars, as reported in [61]. This is to be expected, since even though the initial quadrupole moment is larger for differentially rotating models, the collapse proceeds more slowly, due to the higher values of J/M^2 and this reduces the efficiency in energy emission through gravitational waves. This can also be seen in Fig. 14, where we plot the total energy emitted by gravitational waves, $\Delta E/M$, as a function of J^2/M, which is proportional to the initial axisymmetric quadrupole moment. The triangles represent the uniformly rotating neutron stars discussed in [61], the squares represent the differentially rotating models discussed here, while the solid line is the best fit of the data with the following analytic expression:

$$\frac{\Delta E}{M} = \frac{\left(J^2/M\right)^{n_1}}{a_1\left(J^2/M\right)^{n_2} + a_2},\tag{17}$$

where $a_1 = (5.17 \pm 4.37) \times 10^5$, $a_2 = (1.11 \pm 0.57) \times 10^6$, $n_2 = 2.63 \pm 0.53$, and $n_1 = 1.43 \pm 0.74$. Clearly, because of the small statistics, the error in some of the coefficients is rather large, but this can be compensated by performing additional simulations.

TABLE II: Signal-to-noise ratio (SNR) computed for the collapse of sub-Kerr and supra-Kerr models assuming a source at a distance of $10\,\mathrm{kpc}$. The last column shows also the energy emitted through gravitational waves which, in the case of the sub-Kerr models, is comparable to the one obtained in [61] from the collapse of uniformly rotating neutron stars.

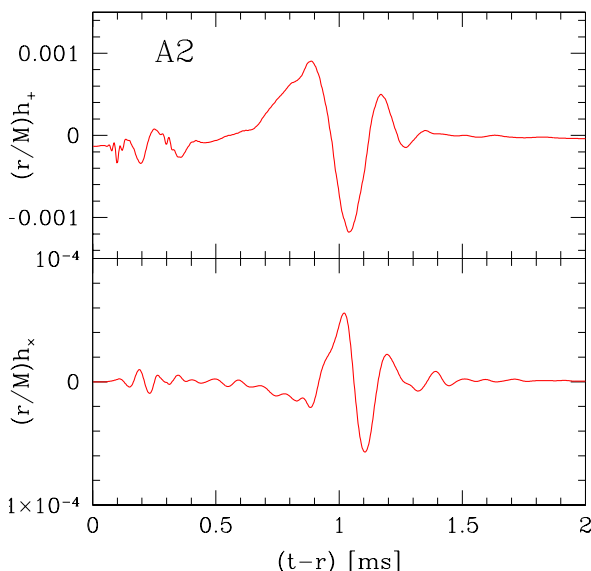| Model	SNR (Virgo)	SNR (LIGO)	SNR (Adv. Virgo)	SNR (Adv. LIGO)	SNR (ET)	$\Delta E/M$
A1	1.00	0.60	3.56	4.80	107.41	5.46×10^{-7}
A2	2.11	1.47	13.98	14.67	246.77	1.38×10^{-7}
A3	4.55	3.79	45.70	47.99	594.54	6.24×10^{-8}
B1	16.13	9.39	45.30	71.75	1688.95	7.89×10^{-4}

FIG. 13: Gravitational-wave amplitudes h_+ (top panel) and $h_\times$ (bottom panel) for the collapse of model A2. The waves are computed using gauge-invariant perturbations of a Schwarzschild spacetime.
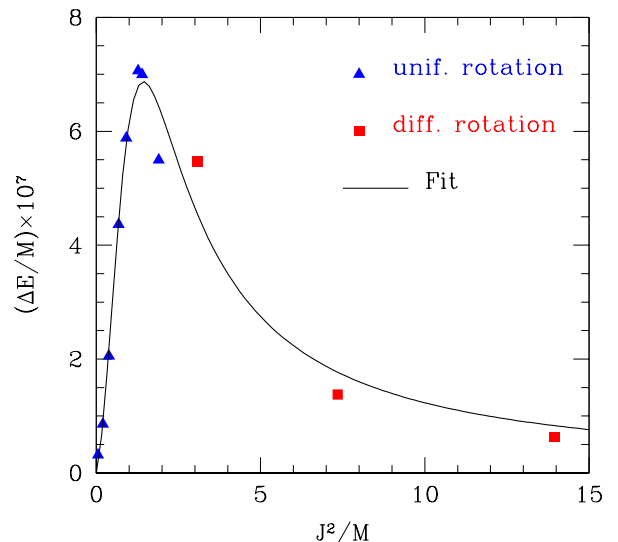

FIG. 14: Energy emitted through gravitational waves, normalized to the total initial mass M, as a function of J^2/M. Triangles represent the uniformly rotating neutron star models studied in [61], while the squares refer to the differentially rotating models discussed here. The solid line is the best fit (see text for details).

B. Supra-Kerr Model

As anticipated in Sec. IV, we have also estimated the gravitational-wave signal emitted by model B1 using the standard quadrupole formula [66, 67] since in this case the outer boundary was not located far enough from the source to allow for the extraction of the signal using the method described in Sec. II D. In this approximation, the observed waveform and amplitude for the two polarizations for an observer situated at large distance r along the z-axis are approximately given by [58]

$$h_+ = \frac{\ddot{I}^{xx}(t) - \ddot{I}^{yy}(t)}{r}, \qquad (18)$$

$$h_\times = 2\,\frac{\ddot{I}^{xy}(t)}{r}, \qquad (19)$$

where

$$I^{jk} = \int d^3x\, D\, x^j x^k \qquad (20)$$

is the quadrupole moment of the matter distribution, $D \equiv \sqrt{\gamma}\rho W$, γ is the determinant of the three metric, and W is the Lorentz factor. The results for the gravitational-wave amplitudes h_+ and $h_\times$ are finally reported in Fig. 15 and they are 1 order of magnitude larger than those emitted by the sub-Kerr models. This produces consequently much larger signal-to-noise ratios as one can see by looking at the last row of table II. As an example, if such a collapse happened at a distance of $10\,\mathrm{kpc}$, we would obtain in the case of advanced LIGO a signal-to-noise ratio of $S/N \approx 72$, with a characteristic amplitude of $h_c = 1.32 \times 10^{-19}(M/M_\odot)$ and at a characteristic frequency $f_c = 2714\,\mathrm{Hz}$. In the case of ET instead the signal could be detected for a source at a distance of up to $\approx 10\,\mathrm{Mpc}$.
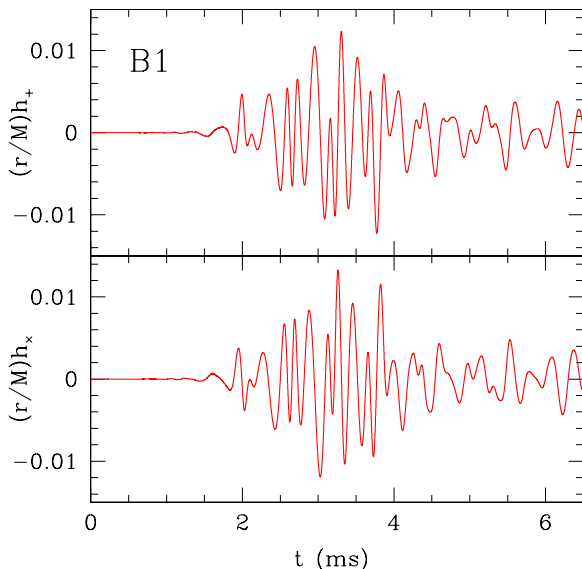
FIG. 15: Gravitational-wave amplitudes h_+ and $h_\times$ for the collapse of model B1. The waves are computed using the Newtonian quadrupole formula.

VI. CONCLUSIONS

We have presented new results on the collapse of differentially rotating neutron stars in full general relativity, using simulations with fixed mesh refinement and in 3D. We have considered two different classes of initial configurations, consisting of either sub-Kerr models with $J/M^2 < 1$, or of supra-Kerr models with $J/M^2 > 1$. In particular, we have performed a detailed study of the parameter space of different equilibrium configurations and, for polytropes which could represent neutron-star models, we could only find models unstable to an axisymmetric instability that are sub-Kerr.

When evolving three representative sub-Kerr models with different degrees of differential rotation we observed in all cases a dynamics which is very similar to the one already found in the case of uniform rotation. In particular, all models remain axisymmetric during collapse and produce a Kerr black hole. We have also studied the collapse of a supra-Kerr model when its collapse is triggered by a 99% depletion of its pressure. In this case, we observed a very different dynamics, with the formation of nonaxisymmetric instabilities, the development of a torus and its subsequent fragmentation in four clumps that merge again, forming a bar and eventually a stable axisymmetric configuration. While lack of evidence cannot be taken to exclude the possibility that a naked singularity can be produced by the collapse of a differentially rotating star, our results also suggest that cosmic censorship is not violated and that rather generic conditions for a supra-Kerr progenitor do not lead to a naked singularity.

For all the models presented here, we have also computed the gravitational-wave signal, which is comparable to the one from uniformly rotating neutron stars. In particular, the efficiency in the emission of gravitational waves for the sub-Kerr models is slightly smaller than the one of uniformly rotating stars. This is due to the large angular momentum that differentially rotating neutron stars have and which increases the time scale on which the collapse happens. Therefore, even if the initial quadrupole moment is much larger, the longer time needed for the collapse decreases the overall efficiency. Furthermore, as for the collapse of uniformly rotating neutron stars, also in this case the detection of such events would be possible only for sources located in our Galaxy in the case of the advanced Virgo and advanced LIGO detectors. However, a third-generation detector such as ET could instead be able to detect a source at a distance of $\sim 1\,\mathrm{Mpc}$.

We plan to extend the work presented here by making use of the axisymmetric code developed in Ref. [68], which will allow us to consider a larger number of models and EOSs. We also plan to investigate the effect that magnetic fields have on these configurations and especially on the supra-Kerr models by using the GRMHD version of Whisky [28]. The magnetic field can in fact redistribute the angular momentum inside the star and thus alter the dynamics of the collapse, as already studied in axisymmetry [20–22] and in 3D [10].

[1] M. Anderson, E. W. Hirschmann, L. Lehner, S. L. Liebling, P. M. Motl, D. Neilsen, C. Palenzuela, and J. E. Tohline, Phys. Rev. D **77**, 024006 (2008).
[2] L. Baiotti, B. Giacomazzo, and L. Rezzolla, Phys. Rev. D **78**, 084033 (2008).
[3] M. Anderson, E. W. Hirschmann, L. Lehner, S. L. Liebling, P. M. Motl, D. Neilsen, C. Palenzuela, and J. E. Tohline, Phys. Rev. Lett. **100**, 191101 (2008).

[4] L. Baiotti, B. Giacomazzo, and L. Rezzolla, Class. Quantum Grav. **26**, 114005 (2009).

[5] Y. T. Liu, S. L. Shapiro, Z. B. Etienne, and K. Taniguchi, Phys. Rev. D **78**, 024012 (2008).

[6] B. Giacomazzo, L. Rezzolla, and L. Baiotti, Mon. Not. R. Astron. Soc. **399**, L164 (2009).

[7] K. Kiuchi, Y. Sekiguchi, M. Shibata, and K. Taniguchi, Phys. Rev. D **80**, 064037 (2009).

[8] E. B. Abdikamalov, C. D. Ott, L. Rezzolla, L. Dessart, H. Dimmelmeier, A. Marek, and H.-T. Janka, Phys. Rev. D **81**, 044012 (2010).

[9] L. Rezzolla, L. Baiotti, B. Giacomazzo, D. Link, and J.-A. Font, Class. Quantum Grav. **27**, 114105 (2010).

[10] B. Giacomazzo, L. Rezzolla, and L. Baiotti, Phys. Rev. D **83**, 044014 (2011).

[11] L. Rezzolla, B. Giacomazzo, L. Baiotti, J. Granot, C. Kouveliotou, and M. A. Aloy, Astrophys. Journ. Lett. **732**, L6 (2011).

[12] T. W. Baumgarte, S. L. Shapiro, and M. Shibata, Astrophys. J. **528**, L29 (2000).

[13] J. L. Friedman, L. Parker, and J. R. Ipser, Astrophys. J. **304**, 115 (1986).

[14] L. Baiotti, I. Hawke, P. J. Montero, F. Löffler, L. Rezzolla, N. Stergioulas, J. A. Font, and E. Seidel, Phys. Rev. D **71**, 024035 (2005).

[15] J. L. Friedman, J. R. Ipser, and R. D. Sorkin, Astrophys. J. **325**, 722 (1988).

[16] K. Takami, L. Rezzolla, and S. Yoshida, MNRAS, *in press* (2011), arXiv:1105.3069.

[17] M. D. Duez, S. L. Shapiro, and H. J. Yo, Phys. Rev. D **69**, 104016 (2004).

[18] M. D. Duez, H. J. Yo, S. L. Shapiro, and B. C. Stephens, Phys. Rev. D **69**, 104030 (2004).

[19] M. D. Duez, Y. T. Liu, S. L. Shapiro, and B. C. Stephens, Phys. Rev. D **72**, 024028 (2005).

[20] M. D. Duez, Y. T. Liu, S. L. Shapiro, M. Shibata, and B. C. Stephens, Physical Review Letters **96**, 031101 (2006).

[21] M. Shibata, M. D. Duez, Y. T. Liu, S. L. Shapiro, and B. C. Stephens, Physical Review Letters **96**, 031102 (2006).

[22] M. D. Duez, Y. T. Liu, S. L. Shapiro, M. Shibata, and B. C. Stephens, Phys. Rev. D **73**, 104015 (2006).

[23] B. C. Stephens, M. D. Duez, Y. T. Liu, S. L. Shapiro, and M. Shibata, Class. Quantum Gravity **24**, S207 (2007).

[24] L. Baiotti, I. Hawke, P. Montero, and L. Rezzolla, in *Computational Astrophysics in Italy: Methods and Tools*, edited by R. Capuzzo-Dolcetta (Mem. Soc. Astron. It., Trieste, 2003), vol. 1, p. 210.

[25] T. Goodale, G. Allen, G. Lanfermann, J. Massó, T. Radke, E. Seidel, and J. Shalf, in *Vector and Parallel Processing – VECPAR'2002, 5th International Conference, Lecture Notes in Computer Science* (Springer-Verlag, Berlin, 2003).

[26] M. Alcubierre, B. Brügmann, T. Dramlitsch, J. Font, P. Papadopoulos, E. Seidel, N. Stergioulas, and R. Takahashi, Phys. Rev. D **62**, 044034 (2000).

[27] L. Baiotti, I. Hawke, L. Rezzolla, and E. Schnetter, Physical Review Letters **94**, 131101 (2005).

[28] B. Giacomazzo and L. Rezzolla, Class. Quantum Grav. **24**, S235 (2007).

[29] R. Arnowitt, S. Deser, and C. W. Misner, in *Gravitation: An Introduction to Current Research*, edited by L. Witten (John Wiley, New York, 1962), pp. 227–265.

[30] T. Nakamura, K.-I. Oohara, and Y. Kojima, Prog. Theor. Phys. Suppl. **90**, 1 (1987).

[31] M. Shibata and T. Nakamura, Phys. Rev. D **52**, 5428 (1995).

[32] T. W. Baumgarte and S. L. Shapiro, Phys. Rev. D **59**, 024007 (1998).

[33] M. Alcubierre, B. Brügmann, P. Diener, M. Koppitz, D. Pollney, E. Seidel, and R. Takahashi, Phys. Rev. D **67**, 084023 (2003).

[34] M. Alcubierre, B. Brügmann, D. Pollney, E. Seidel, and R. Takahashi, Phys. Rev. D **64**, 61501 (R) (2001).

[35] L. Baiotti and L. Rezzolla, Physical Review Letters **97**, 141101 (2006).

[36] H.-O. Kreiss and J. Oliger, GARP Pub. Series **10** (1973).

[37] F. Banyuls, J. A. Font, J. M. Ibáñez, J. M. Martí, and J. A. Miralles, Astrophys. J. **476**, 221 (1997).

[38] J. A. Font, Living Rev. Relativity **11**, 7 (2008).

[39] J. M. Martí and E. Müller, Living Rev. Relativity **6**, 7 (2003).

[40] L. Rezzolla and O. Zanotti, J. Fluid. Mech. **449**, 395 (2001).

[41] L. Rezzolla, O. Zanotti, and J. A. Pons, J. Fluid. Mech. **479**, 199 (2003).

[42] P. Colella and P. R. Woodward, J. Comput. Phys. **54**, 174 (1984).

[43] E. Schnetter, S. H. Hawley, and I. Hawke, Class. Quantum Grav. **21**, 1465 (2004).

[44] M. J. Berger and J. Oliger, J. Comput. Phys. **53**, 484 (1984).

[45] M. E. Rupright, A. M. Abrahams, and L. Rezzolla, Phys. Rev. D **58**, 044005 (1998).

[46] K. Camarda and E. Seidel, Phys. Rev. D **59**, 064019 (1999).

[47] V. Moncrief, Annals of Physics **88**, 323 (1974).

[48] A. Nagar and L. Rezzolla, Class. Quantum Gravity **22**, R167 (2005).

[49] A. Nagar and L. Rezzolla, Class. Quantum Gravity **23**, 4297 (2006).

[50] N. Stergioulas and J. L. Friedman, Astrophys J. **444**, 306 (1995).

[51] T. Nozawa, N. Stergioulas, E. Gourgoulhon, and Y. Eriguchi, Astron. Astrophys. Suppl. Ser. **132**, 431 (1998).

[52] N. Stergioulas, Living Rev. Relativity **6**, 3 (2003).

[53] H. Komatsu, Y. Eriguchi, and I. Hachisu, MNRAS **237**, 355 (1989).

[54] F. Galeazzi, S. Yoshida, and Y. Eriguchi, ArXiv e-prints (2011), 1101.2664.

[55] J. Thornburg, Class. Quantum Gravity **21**, 743 (2004).

[56] M. Thierfelder, S. Bernuzzi, D. Hilditch, B. Bruegmann, and L. Rezzolla, Phys. Rev. D **83**, 064022 (2011).

[57] L. Baiotti, T. Damour, B. Giacomazzo, A. Nagar, and L. Rezzolla, Phys. Rev. Lett. **105**, 261101 (2010).

[58] L. Baiotti, R. De Pietri, G. M. Manca, and L. Rezzolla, Phys. Rev. D **75**, 044023 (2007).

[59] G. M. Manca, L. Baiotti, R. D. Pietri, and L. Rezzolla, Class. Quantum Grav. **24**, S171 (2007).

[60] J. K. Truelove, R. I. Klein, C. F. McKee, J. H. Holliman, II, L. H. Howell, and J. A. Greenough, Astrophys. J. **489**, L179 (1997).

[61] L. Baiotti, I. Hawke, and L. Rezzolla, Class. Quantum Grav. **24**, S187 (2007).

[62] C. T. Cunningham, R. H. Price, and V. Moncrief, Astrophys. J. **230**, 870 (1979).

[63] E. Seidel, Phys. Rev. D **42**, 1884 (1990).

[64] E. Seidel, Phys. Rev. D **44**, 950 (1991).

[65] M. Punturo et al., Class. Quantum Grav. **27**, 084007 (2010).

[66] A. Nagar, O. Zanotti, J. A. Font, and L. Rezzolla, Phys. Rev. D **75**, 044016 (2007).

[67] L. Baiotti, S. Bernuzzi, G. Corvino, R. De Pietri, and A. Nagar, Phys. Rev. D **79**, 024002 (2009).

[68] T. Kellerman, L. Baiotti, B. Giacomazzo, and L. Rezzolla, Class. Quantum Grav. **25**, 225007 (2008).